A Unified Metric for Fast Frequency Response in Low-Inertia Power Systems

Preprint

Xiaofan Cui,[1,2] Shuan Dong,[1] Andy Hoke,[1] and Jin Tan[1]

1 National Renewable Energy Laboratory
2 University of Michigan

To be Presented at the 2023 IEEE Conference on Innovative Smart Grid Technologies North America (ISGT NA)
Washington, D.C.
January 16–19, 2023

NREL is a national laboratory of the U.S. Department of Energy
Office of Energy Efficiency & Renewable Energy
Operated by the Alliance for Sustainable Energy, LLC

This report is available at no cost from the National Renewable Energy Laboratory (NREL) at www.nrel.gov/publications.

Contract No. DE-AC36-08GO28308

Conference Paper
NREL/CP-6A40-81409
December 2022

A Unified Metric for Fast Frequency Response in Low-Inertia Power Systems

Preprint

Xiaofan Cui,[1,2] Shuan Dong,[1] Andy Hoke,[1] and Jin Tan[1]

1 National Renewable Energy Laboratory
2 University of Michigan

Suggested Citation
Cui, Xiaofan, Shuan Dong, Andy Hoke, and Jin Tan. 2022. *A Unified Metric for Fast Frequency Response in Low-Inertia Power Systems: Preprint*. Golden, CO: National Renewable Energy Laboratory. NREL/CP-6A40-81409.
https://www.nrel.gov/docs/fy23osti/81409.pdf.

NREL is a national laboratory of the U.S. Department of Energy
Office of Energy Efficiency & Renewable Energy
Operated by the Alliance for Sustainable Energy, LLC

This report is available at no cost from the National Renewable Energy Laboratory (NREL) at www.nrel.gov/publications.

Contract No. DE-AC36-08GO28308

Conference Paper
NREL/CP-6A40-81409
December 2022

National Renewable Energy Laboratory
15013 Denver West Parkway
Golden, CO 80401
303-275-3000 • www.nrel.gov

NOTICE

This work was authored in part by the National Renewable Energy Laboratory, operated by Alliance for Sustainable Energy, LLC, for the U.S. Department of Energy (DOE) under Contract No. DE-AC36-08GO28308. Funding provided by U.S. Department of Energy Office of Energy Efficiency and Renewable Energy Solar Energy Technologies Office Award Number 37772. The views expressed herein do not necessarily represent the views of the DOE or the U.S. Government.

A Unified Metric for Fast Frequency Response in Low-Inertia Power Systems

Xiaofan Cui[1,2], *Student Member, IEEE,* Shuan Dong[1], *Member, IEEE,* Andy Hoke[1], *Senior Member, IEEE,* Jin Tan* [1], *Senior Member, IEEE*

1. National Renewable Energy Laboratory, Golden, CO, USA

2. Department of EECS, University of Michigan, Ann Arbor

***Abstract*— Future power systems with more inverter-based resources (IBRs), will be vulnerable to frequency decline contingencies. Fast frequency response (FFR) provided by IBRs is a good candidate to arrest frequency excursions. Diverse types of FFR have been proposed, and some have been deployed in our power systems. Without a unified quantification of FFR, it is hard for the grid operators to compare and fully leverage the FFR capabilities of IBRs. This work introduces a potential unified metric that quantifies two key characteristics of FFR and describes its application to three prevailing FFR types. We then use metric-to-frequency mapping to validate the accuracy of the metric in predicting the impact of a given FFR on the trajectory of a frequency event. The results show that the proposed metric is simple yet accurately captures the ability of diverse forms of FFR to improve system frequency dynamics.**

Keywords—fast frequency response, metrics, low-inertia grid, effective inertia, frequency stability

I. INTRODUCTION

On the road to a future power system with 100% penetration of renewable energy, increasingly lower penetrations of synchronous generators (SGs) cause a huge drop in the rotational inertia and primary frequency response (PFR) capability [1]. Consequently, system frequency fluctuations in response to power disturbances can trigger underfrequency load shedding [2]. High-bandwidth control of inverter-based resources (IBRs) can enable fast frequency response (FFR), which can help relieve this frequency instability problem if intelligently deployed [3].

The quantification of FFR to allow diverse forms of FFR to be optimally deployed by grid operators is not adequately addressed. A conventional understanding of FFR is that a faster, bigger, and longer FFR can better support the frequency [4]; however, this qualitative understanding is not enough to help grid operators deploy FFR capability systematically, especially considering that several forms of FFR have been proposed. Without uniform quantification of FFR, 1) the net cost of FFR services increases because grid schedulers might assign nonoptimal output power to FFR providers, and 2) frequency stability is not guaranteed because the mapping from the amounts and types of FFR to the frequency nadir is unknown.

Simple and accurate metrics are needed to quantitively capture the ability of a FFR trajectory to improve system frequency dynamics. One challenge is that diverse forms of FFR differ in their response speed, duration, exit mechanism, etc. More research is needed to quantify the effects of different types of FFR in a unified manner. Here, we focus on three types of FFR that we refer to as *step FFR*, *proportional FFR*, and *derivative FFR* [3]. Step FFR, which boosts the active power by a predetermined fixed amount, is used in the Siemens Gamesa wind turbine generators (WTGs) [3] and some battery energy storage systems. Proportional FFR, which increases active power by an amount proportional to the frequency deviation, has been implemented in a GE photovoltaic plant, Enercon WTGs, and other IBRs [3]. Derivative FFR, which emulates synchronous machine inertial response by increasing power in proportion to the rate of change of frequency (RoCoF), can be provided by some battery energy storage systems from Tesla [3], for example. These prevailing FFRs are different in response speed, magnitude, and response duration.

Most existing FFR metrics are limited to only one form of FFR. Reference [5] quantifies the contribution of derivative FFR in terms of RoCoF reduction. References [7] and [8] use the droop coefficient to quantify the contribution of proportional FFR to the frequency nadir. Step FFR is rarely quantified in previous papers. Given a system with multiple possible FFR types, it is hard to evaluate the performance of each FFR type without unified metrics.

The Electric Reliability Council of Texas [9] proposed to quantify FFR by comparison to SG response. To achieve the same frequency nadir, one unit of FFR can be equated to m units of SGs. This metric, m, is advantageous in its wide compatibility to all different types of FFR; however, there are two disadvantages: 1) m varies with different systems and operating points, and hence it is hard to generalize; 2) m only quantifies the FFR capability of improving the nadir. Other FFR capabilities, such as improving the RoCoF, are not captured.

The contributions of this paper include the following: 1) We propose a unified metric that can be applied to all forms of FFR and exemplify its application to step FFR. 2) We show an approach to validate the accuracy of the metric by mapping it to key frequency response characteristics, called metric-to-frequency mapping. The results show the proposed metric to be a simple yet accurate predictor of the effects of FFR on frequency trajectory.

II. UNIFIED METRIC FOR FFR

A. Comparisons Among Prevailing FFR Trajectories

FFR is the power injected to (or absorbed from) the grid in response to variations in the measured grid frequency [3]. FFR

usually acts during the arresting phase of a frequency excursion event, and its design goal is to improve the initial RoCoF and/or frequency nadir.

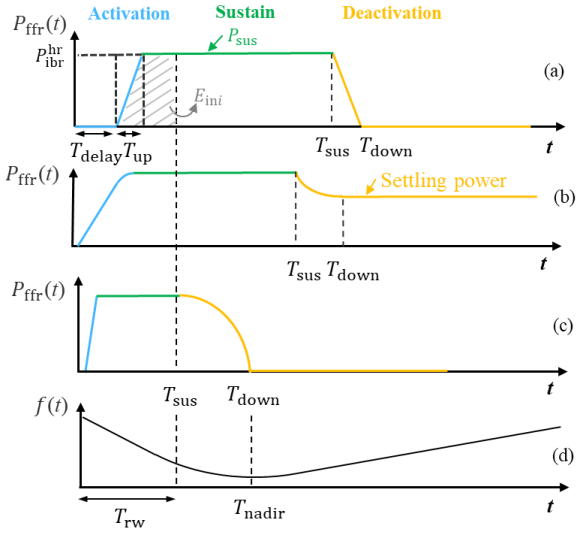

Fig. 1. Power trajectories of three prevailing FFRs: a) step FFR, b) proportional FFR, c) derivative FFR, and d) system frequency.

FFR types are hard to unify because of diverse types of response trajectories. In this paper, we focus on three prevailing FFR types in the industry: step FFR, proportional FFR, and derivative FFR, as shown in Fig. 1(a), (b), and (c), respectively. As shown in Fig. 1, all three FFR power trajectories, $P_{\text{ffr}}(t)$, consist of three phases: activation, sustaining, and deactivation, highlighted in blue, green, and orange colors, respectively.

1) Activation Phase: The activation phase starts from the triggering event contingency and ends when the FFR is fully activated. The step FFR needs a delay to evaluate the contingency before it ramps up. The trajectory can be modeled by the parameters of delay time, T_{delay}, linear ramp-up time, T_{up}, and magnitude of response, P_{ibr}^{hr}. The proportional FFR in Fig. 1(b) ramps up in proportion to the frequency deviation. The derivative FFR in Fig. 1(c) steps up the fastest among the three, but this will depend on the FFR control parameters and the frequency profile.

2) Sustaining Phase: The sustaining phase describes the period when the FFR is fully activated. In general, the peak FFR power magnitude can vary for different frequency event trajectories. However, for the purposes of quantifying FFR, we assume the FFR is designed to fully exploit the scheduled power headroom, $P_{\text{ibr}}^{\text{hr}}$, during the largest generation loss event; otherwise, the scheduling is not economic. Therefore, the power trajectory during the sustaining phase is a horizontal plateau at maximum power.

3) Deactivation phase: The deactivation phase represents the exit procedure of the FFR. Proportional FFR starts to deactivate when the system frequency begins to recover. The settling power of proportional FFR is determined by the steady-state frequency deviation. Derivative FFR starts to deactivate after the SGs start to provide PFR and is fully deactivated when the frequency reaches the nadir.

To summarize the observations: 1) the activation phases of the three FFR types are different according to the shape of their response trajectories; 2) the deactivation phase of derivative FFR ends at the frequency nadir when the other two FFR types can still be in their sustaining phases; and 3) for a worst-case frequency event the sustaining phases of all three types of FFR plateau at maximum power.

B. Development of FFR Metric

A good metric of FFR should capture the major impacts of FFR on the frequency trajectory and be concise. Our proposed metric has two dimensions: initial FFR energy, E_{ini}, and sustaining power, P_{sus}. The initial FFR energy, E_{ini}, is defined as the integral of the FFR power trajectory, $P_{\text{ffr}}(t)$, in the RoCoF window, T_{rw}:

$$E_{\text{ini}} = \int_0^{T_{\text{rw}}} P_{\text{ffr}}(t)dt \tag{1}$$

where T_{rw} is system specific. Here, we choose T_{rw} based on a pure SGs system, which is the same as the actual system under study except all FFR is disabled. The RoCoF time window, T_{rw}, is defined as the period when the SGs provide zero PFR. FFR can respond more quickly to the frequency decline than SGs' PFR; therefore, it is reasonable to assume that the FFR can be fully activated during the RoCoF time window. Initial energy, E_{ini}, quantifies how fast and how much the FFR responds to the contingency during the activation phase. Compared to an alternative representation using delay, response trajectory, and power delivery, initial energy is advantageous in its simplicity. The complicated startup procedure is aggregated into a simple energy term. High initial energy indicates a fast-response FFR service, which can arrest the frequency excursion rapidly.

We present an example of the quantification of a step FFR using E_{ini}. The power trajectory can be modeled in Fig. 1 with the parameters of delay time, T_{delay}; linear ramp-up time, T_{up}; and magnitude of response, $P_{\text{ibr}}^{\text{hr}}$. Based on (1), the step FFR can be quantified as

$$E_{\text{ini}} = \left(T_{\text{rw}} - T_{\text{delay}} - \frac{T_{\text{up}}}{2}\right) P_{\text{ibr}}^{\text{hr}} \tag{2}$$

The relationship between step FFR trajectories and the E_{ini} and P_{sus} metrics is shown in Fig. 2. Short T_{delay} and T_{up} result in high E_{ini}. Large IBR headroom increases both E_{ini} and P_{sus}.

In the sustaining phase, the P_{sus} metric is expected to describe the FFR magnitude and how long it lasts. Therefore, the sustaining power, P_{sus}, represents the power that a fully activated FFR can sustain until the frequency nadir instant, T_{nadir}. P_{sus} varies for different types of FFR. For the step and proportional FFR, the following equation holds:

$$P_{\text{sus}} = P_{\text{ibr}}^{\text{hr}} \tag{3}$$

Step FFR provided by battery energy storage systems can commonly sustain over 10 seconds, which is longer than the largest T_{nadir}. Proportional FFR does not deactivate until the frequency nadir comes. For derivative FFR, we have P_{sus}=0, because this type of FFR starts to be deactivated right after T_{rw} and will be fully deactivated at T_{nadir} when df/dt = 0.

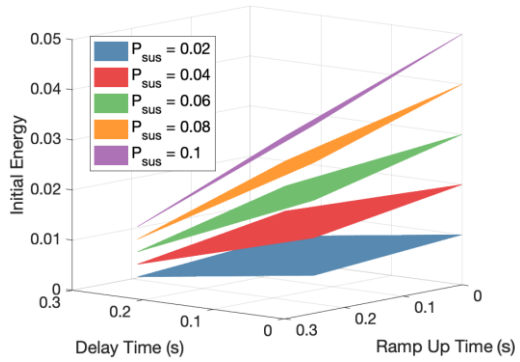

Fig. 2. Mapping from the step FFR trajectories to the FFR metric.

We choose P_{sus} as part of the metric because it is closely related to the headroom, $P_{\text{ibr}}^{\text{hr}}$, the decision variable in grid scheduling. High sustaining power indicates better ability to fill in the power gap caused by the generation loss.

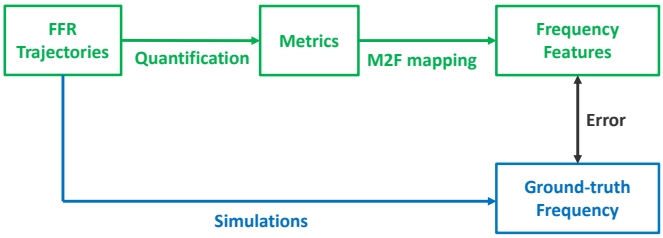

Fig. 3. FFR metric validation procedure.

III. Validation of Metrics

This section shows an approach to validate the accuracy of the FFR metric called metric-to-frequency mapping (see Fig. 3). Metric-to-frequency mapping is defined as the mapping from the FFR metrics to key frequency features for the largest credible contingency. Recall that the metric quantification step has been described in Section II. Here, we derive the metric-to-frequency mapping in Sections III-A and III-B and discuss the simulation steps in Sections III-C and III-D.

The time-varying FFR power injection causes difficulties in the analytical approach. Because of the nonnegligible dynamics in FFR, the system order is elevated. The existing work tends to incorporate the FFR into the system dynamics, which causes difficulties in analysis and unification. To avoid these issues, we treat the FFR trajectory as an external power injection into the system.

A. Response Decomposition

We demonstrate a new *response decomposition* method to derive the metric-to-frequency mapping. The power system dynamics becomes complicated because of the time-varying FFR power trajectory. The existing works [7][8] combine the FFR dynamics and the synchronous generators dynamics, which increase the complexity in analyzing the system dynamics. Instead, we treat the FFR trajectory as an external power injection to the system. The frequency trajectory of the system follows the below modified swing equation:

$$2H_{\text{sg}}\frac{\mathrm{d}f}{\mathrm{d}t} = P_{\text{gen}} - P_{\text{load}} - P_{\text{genloss}} + P_{\text{ffr}} \tag{4}$$

where P_{gen} is the generator power trajectory, P_{load} is the load power trajectory, P_{genloss} represents the generation loss in the contingency, and P_{ffr}, as shown in Fig. 4(a) is a step FFR trajectory.

Ideally, FFR is expected to support the power gap as soon as the contingency happens, as shown in Fig. 4(b); however, because of the delay and dynamics that occurred during activation, the actual FFR power trajectory follows Fig. 4(a). Therefore, we decompose the actual FFR power trajectory, P_{ffr}, as the ideal power trajectory $\bar{P}_{\text{ffr}}$ plus the mismatched power trajectory $\hat{P}_{\text{ffr}}$ as follows. The mismatched power trajectory is shown in Fig. 4(c)

$$\hat{P}_{\text{ffr}} = P_{\text{ffr}} - \bar{P}_{\text{ffr}}. \tag{5}$$

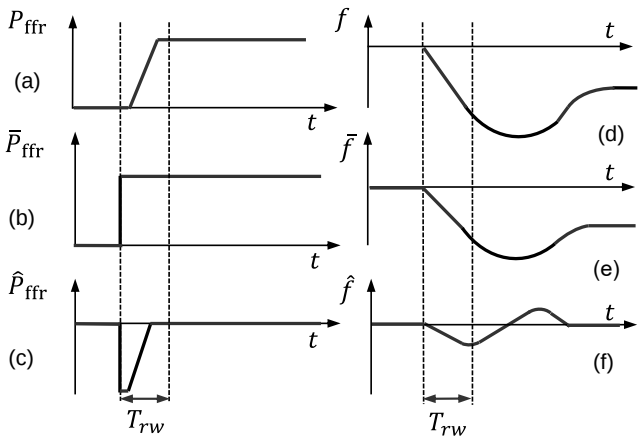

Fig. 4. (a) Actual FFR power trajectory; (b) ideal FFR power trajectory; (c) mismatched FFR power trajectory; (d)frequency trajectory of the system with actual FFR; (e) frequency trajectory of the system with ideal FFR; (f) frequency trajectory of the system with mismatched FFR.

Similarly, we decompose the frequency trajectory $f(t)$ and generator power trajectory $P_{\text{gen}}(t)$ of the system with actual FFR as the superposition of the frequency trajectory $\bar{f}(t)$ and generator power trajectory $\bar{P}_{\text{gen}}(t)$ with ideal FFR

$$2H_{\text{sg}}\frac{\mathrm{d}\bar{f}}{dt} = \bar{P}_{\text{gen}} - P_{\text{load}} - P_{\text{genloss}} + \bar{P}_{\text{ffr}}, \tag{6}$$

and the frequency trajectory $\hat{f}(t)$ and generator power trajectory $\hat{P}_{\text{gen}}(t)$ of the system with mismatched FFR

$$2H_{\text{sg}}\frac{\mathrm{d}\hat{f}}{\mathrm{d}t} = \hat{P}_{\text{gen}} + \hat{P}_{\text{ffr}}(t). \tag{7}$$

The frequency trajectory $f(t)$ of system with actual FFR, the frequency trajectory $\bar{f}(t)$ of the system with ideal FFR, and the frequency trajectory $\hat{f}(t)$ of the system with mismatched FFR are illustrated in Fig. 4(d), (e), and (f), respectively.

The RoCoF can be decomposed as (8) because of the linearity

$$RoCoF = \overline{RoCoF} + \widehat{RoCoF}. \tag{8}$$

The frequency deviation can be decomposed as (9)

$$\Delta f_{\text{nadir}} = \left(\Delta\bar{f}(t) + \Delta\hat{f}(t)\right)_{\min}. \quad (9)$$

Because the minimization function is super-linear, we have

$$\Delta f_{\text{nadir}} \geq \Delta\bar{f}_{\text{nadir}} + \Delta\hat{f}_{\text{nadir}}. \quad (10)$$

From (10), we can guarantee the worst-case frequency deviation by bounding the frequency deviation of the system with ideal FFR and the frequency deviation of the system with mismatched FFR separately.

B. Metric-to-frequency Mapping of Step FFR

The metric-to-frequency mapping of step FFR can be derived based on the *response-decomposition* method. The resulting metric-to-RoCoF mapping of the system is linear with the metric E_{ini}

$$RoCoF = a_0 E_{\text{ini}} + a_1 P_{\text{genloss}}, \quad (11)$$

Where $a_0 = \frac{1}{2H_{\text{sg}}T_{\text{rw}}}$ and $a_1 = -\frac{1}{2H_{\text{sg}}}$.

Equation (11) can be derived from (8), (12), and (13). Equation (12) is the RoCoF of the system with ideal FFR, and (13) is the RoCoF of the system with mismatched FFR

$$\overline{RoCoF} = \frac{P_{\text{sus}}T_{\text{rw}} - P_{\text{genloss}}\,T_{\text{rw}}}{2H_{\text{sg}}T_{\text{rw}}}, \quad (12)$$

$$\widehat{RoCoF} = \frac{\int_0^{T_{\text{rw}}} P_{\text{ffr}}(t)dt - P_{\text{sus}}T_{\text{rw}}}{2H_{\text{sg}}T_{\text{rw}}}. \quad (13)$$

The metric-to-frequency deviation mapping follows

$$\Delta f_{\text{nadir}} \geq (P_{\text{sus}} - P_{\text{genloss}})R_{\text{sg}} - A\sqrt{1-\xi^2}\,e^{-\frac{\delta}{2T_{\text{sg}}\omega_d}} \quad (14)$$

where

$$\omega_d = \sqrt{\frac{1}{2R_{\text{sg}}T_{\text{sg}}H_{\text{sg}}} - \frac{1}{4T_{\text{sg}}^2}}, \qquad \xi = \sqrt{\frac{R_{\text{sg}}H_{\text{sg}}}{2T_{\text{sg}}}}$$

$$\delta = \arcsin\left(\frac{\sin(\theta_2 - \omega_d T_{\text{rw}} - \theta_1)}{\sin\theta_1}\frac{(P_{\text{genloss}} - P_{\text{sus}})R_{\text{sg}}}{A}\right) + \omega_d T_{\text{rw}},$$

$$A = \sqrt{A_1^2 + A_2^2 + 2A_1A_2\cos(\theta_2 - \omega_d T_{rw} - \theta_1)},$$

$$A_1 = \frac{(P_{\text{genloss}} - P_{\text{sus}})R_{\text{sg}}}{\sin\theta_1}, \quad A_2 = \frac{P_{\text{sus}}T_{\text{rw}} - E_{\text{ini}}}{2H_{\text{sg}}\sqrt{1-\xi^2}}e^{\frac{T_{\text{rw}}}{2T_{\text{sg}}}},$$

$$\theta_1 = \arctan\left(\frac{2\sqrt{1/\xi^2 - 1}}{2 - 1/\xi^2}\right), \quad \theta_2 = \pi + \arccos\xi.$$

R_{sg} is the droop coefficient of the governor. T_{sg} is the time constant of the SG governor and turbine. (14) can be derived from (9), (15), and (16). Below, (15) is the frequency deviation of the system with ideal FFR, and (16) bounds the frequency deviation of the system with mismatched FFR from below.

$$\Delta\bar{f}(t) = (P_{\text{sus}} - P_{\text{genloss}})R_{sg}\left(1 - \frac{e^{-\frac{t}{2T_{\text{sg}}}}}{\sin\theta_1}\sin(\omega_d t + \theta_1)\right) \quad (15)$$

$$\Delta\hat{f}(t) \geq \frac{E_{\text{ini}}}{2H_{\text{sg}}}\frac{e^{-\frac{t-T_{\text{rw}}}{2T_{\text{sg}}}}}{\sqrt{1-\xi^2}}\sin(\omega_d(t - T_{\text{rw}}) + \theta_2) \quad (16)$$

This metric-to-frequency mapping is not only significant in validating metrics but also in evaluating the contributions of different FFR types to system frequency trajectories. The frequency metrics are calculated for a worst-case frequency trajectory. Conversely, a set of security constraints on the frequency trajectory can be mapped back to a set of constraints on the FFR metrics. The metric-to-frequency mapping provides a security guarantee and engineering insights, and it could be incorporated with grid scheduling. With this property, a grid operator could evaluate the adequacy of FFR capability by checking whether the resulting worst-case frequency trajectory is safe. A grid scheduler can obtain the FFR reserve constraints from the frequency-security constraints.

C. Simulation Setup

Table 1 Key parameters of the test system in the 50% IBR penetration case

V_{gene} (line to line)	24 kV	Generator Inertia	6 s
V_{trans} (line to line)	230 kV	Droop Coefficient	5 %
Generator Power	0.5 pu	Friction Coefficient	0.1 %
IBR power	0.5 pu	Nominal Frequency	60 Hz
Load Active Power	1 pu	Load Sensitivity	1 %
Load Active Power	0.1 pu	Turbine Time Const.	0.6 s
Nominal Power	300 MW	Governor Time Const.	0.3 s
Generator Trip	30 MW at 20 s	RoCoF Window	0.5 s

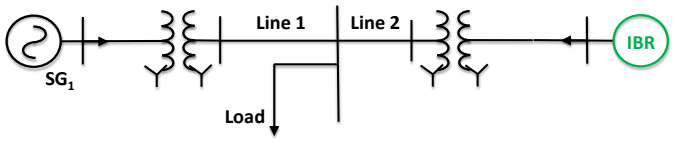

Fig. 5 EMT model of a 3-bus system with a synchronous generator (SG), inverter-based resource (IBR), and constant-power load.

In this section, we complete the validation procedures by comparing the frequency features obtained from analytical metric-to-frequency mapping with the ground truth from the time-domain simulations. The simulation is performed on a three-bus test system with a SG, an IBR, and a constant-power load, as shown in Fig. 5. The SG is equipped with turbine-governor droop control and an exciter. The key parameters of the test system are shown in Table 1. A load step change is applied to equivalently emulate the generator trip contingency. The renewable penetration level can be adjusted by tuning the IBR and SG output power.

D. Validation by Comparing Metric-to-frequency and Simulations

A series of step FFR trajectories with different delay times, ramp-up times, sustaining powers, and renewable penetration ratios, α, were studied following the metric validation

procedure in Fig. 3. For each trajectory, E_{ini} and P_{sus} were quantified. The analytical metric-to-frequency mapping in Section III was used to map the metrics to the RoCoF and the frequency nadir. These frequency features were also extracted from the simulated frequency trajectory. The RoCoF is calculated as the average slope of the frequency trajectory during the first 0.5 s after the contingency, and the frequency nadir is obtained at the first local minimum point of the frequency trajectory after the contingency. An accurate metric will result in small differences between the RoCoF/frequency nadir from the analytical metric-to-frequency mapping and those from the power system simulation.

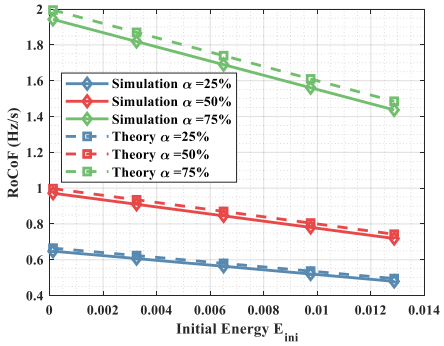

Fig. 6. Validation of metrics by comparing metric-to-RoCoF mapping to simulations.

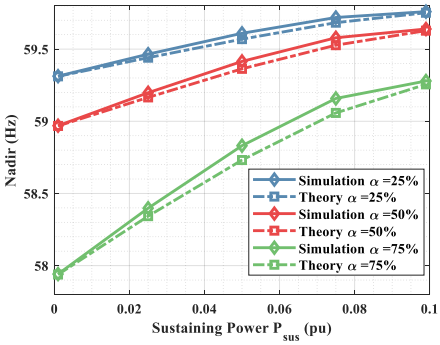

Fig. 7. Validation of metrics by comparing metric-to-nadir mapping to simulations.

Fig. 6 compares the RoCoFs from the simulation and the analytical metric-to-frequency mapping. High renewable penetration, α, significantly increases the RoCoF, and high E_{ini} decreases the RoCoF. P_{sus} does not affect the RoCoF, as expected. The RoCoFs from the analytical matric-to-frequency mapping, as shown by the dashed lines, form tight worst-case bounds of the ground-truth RoCoFs, as shown by the solid lines. The error is small and less than 50 mHz/s, which validates the accuracy of the metrics in capturing all key impact factors to the RoCoF. The cause of the error is that analytical metric-to-frequency mapping assumes that the SG provides zero response during the RoCoF window; however, the actual response of the SG is slightly nonzero.

Fig. 7 compares the frequency nadirs from the simulation and the analytical metric-to-frequency mapping. High P_{sus} and low α significantly increase the nadir. The nadirs from the analytical M2P mapping, as shown by the dashed lines, are tight worst-case bounds of the ground-truth nadirs, as shown in the solid lines. The error is small and less than 100 mHz, which validates the accuracy of the metric in capturing all key impact factors on the frequency nadir. The error is caused by the zero SG response assumption during the RoCoF window.

IV. Conclusion

This paper defines and explains the usefulness of a unified and accurate metric for accessing FFR capabilities from IBRs which is critical to ensure the frequency stability of a low-inertia grid suffering large energy imbalance. The newly proposed two-part metric can be applied to various types of FFR and easily map to the key parameters of frequency trajectory including RoCoF and frequency nadir. A systematic validation approach of FFR metrics has been proposed through metric-to-frequency mapping. The accuracy of the proposed metric is comprehensively validated. The proposed metric is useful for operating and planning a grid with increased amounts of renewables by accessing the FFR contributions from various resources. This can potentially enable grid operators to effectively schedule diverse types of FFR services and improve frequency stability.

Acknowledgments

This work was authored in part by the National Renewable Energy Laboratory, operated by Alliance for Sustainable Energy, LLC, for the U.S. Department of Energy (DOE) under Contract No. DE-AC36-08GO28308. This material is based upon work supported by the U.S. Department of Energy's Office of Energy Efficiency and Renewable Energy (EERE) under the Solar Energy Technologies Office Award Number 37772. The U.S. Government retains and the publisher, by accepting the article for publication, acknowledges that the U.S. Government retains a nonexclusive, paid-up, irrevocable, worldwide license to publish or reproduce the published form of this work, or allow others to do so, for U.S. Government purposes. The views expressed herein do not necessarily represent the views of the U.S. Department of Energy or the United States Government.

References

[1] B. Hartmann, I. Vokony, and I. Táczi, "Effects of decreasing synchronous inertia on power system dynamics—Overview of recent experiences and marketisation of services," *Int. Trans. Electr. Energy Syst.*, 2019.
[2] F. Milano, F. Dorfler, G. Hug, D. J. Hill, and G. Verbič, "Foundations and challenges of low-inertia systems (Invited Paper)," in *20th Power Systems Computation Conference, PSCC 2018*, 2018.
[3] NERC, "Fast Frequency Response Concepts and Bulk Power System Reliability Needs," 2020.
[4] N. Modig *et al.*, "Technical Requirements for Fast Frequency Reserve Provision in the Nordic Synchronous Area," 2019.
[5] M. Kosmecki *et al.*, "A methodology for provision of frequency stability in operation planning of low inertia power systems," *Energies*, 2021.
[6] Q. Wang, F. Li, Y. Tang, and Y. Xu, "Integrating Model-Driven and Data-Driven Methods for Power System Frequency Stability Assessment and Control," *IEEE Trans. Power Syst.*, vol. 34, no. 6, pp. 4557–4568, 2019.
[7] H. Li, Y. Qiao, Z. Lu, B. Zhang, and F. Teng, "Frequency Constrained Stochastic Planning Towards a High Renewable Target Considering Frequency Response Support from Wind Power," *IEEE Trans. Power Syst.*, 2021.
[8] Z. Zhang, E. Du, F. Teng, N. Zhang, and C. Kang, "Modeling Frequency Dynamics in Unit Commitment with a High Share of Renewable Energy," *IEEE Trans. Power Syst.*, vol. 35, no. 6, pp. 4383–4395, 2020.
[9] W. Li, P. Du, and N. Lu, "Design of a new primary frequency control market for hosting frequency response reserve offers from both generators and loads," IEEE Trans. Smart Grid, vol. 9, no. 5, pp. 4883–48